Corrosion resistance of steel reinforcement in carbonated reactive magnesia cement-based mixes with different Portland cement contents

Mi, Tangwei; Yang, En-Hua; Unluer, Cise

Published in:
Cement and Concrete Composites

DOI:
10.1016/j.cemconcomp.2024.105668

Publication date:
2024

Cement and Concrete Composites 152 (2024) 105668

Contents lists available at ScienceDirect

Cement and Concrete Composites

journal homepage: www.elsevier.com/locate/cemconcomp

Corrosion resistance of steel reinforcement in carbonated reactive magnesia cement-based mixes with different Portland cement contents

Tangwei Mi [a], En-Hua Yang [a], Cise Unluer [b,*]

[a] School of Civil and Environmental Engineering, Nanyang Technological University, 50 Nanyang Avenue, 639798, Singapore
[b] Department of Mechanical, Aerospace and Civil Engineering, University of Manchester, Manchester, M13 9PL, United Kingdom

ARTICLE INFO

Keywords:
MgO
Reinforcement
Corrosion
Spectroscopy
Carbonation

ABSTRACT

Carbonated reactive magnesia cement (RMC)-based mixes raise questions about the corrosion resistance of reinforcement. This study investigated steel reinforcement behaviour in RMC-based mixtures containing 2 % (M98) and 20 % (M80) Portland cement (PC), compared to 100 % PC (M0). Response to carbonation curing through electrochemical measurements, changes in OH^- content, chemical composition and microstructure within carbonated pastes were reported. Reduced porosity with increased PC content before carbonation was attributed to distinct pore structures of hydrated RMC/PC mixes. Calcite was the primary carbonation product in all, with nesquehonite and hydromagnesite detected in M98 and M80. Steel reinforcement in M98 exhibited corrosion, while that in M80 displayed corrosion resistance comparable to M0, which remained passivated even under carbonation conditions. Microstructure densification via the formation of carbonation products proved insufficient in preventing further carbonation in M98 due to its high porosity. Corrosion of reinforcement in M98 was ascribed to its relatively high porosity and low OH^- content. Valuable insights for optimizing carbonated RMC-based mixtures for structural applications were provided.

1. Introduction

Production of Portland cement (PC) leads to substantial carbon dioxide (CO_2) emissions globally [1], promoting increased attention to alternative binder systems with lower environmental impacts. Reactive MgO cement (RMC) is considered as a promising alternative binder to PC due to its potential of being less CO_2-intensive than PC, depending on the production and curing conditions [2–5]. There are two major routes for the production of RMC, including dry and wet routes. For the dry route, a calcination temperature, 700–1000 °C, is normally required, which is much lower than temperatures required for the production for PC, resulting in less energy consumption [5]. Additionally, RMC is capable to be recycled from waste resources with high Mg concentrations like reject brine [6]. Furthermore, RMC can gain strength by sequestering CO_2 through the carbonation reaction, resulting in the formation of hydrated magnesium carbonates (HMCs), such as nesquehonite ($MgCO_3{\cdot}3H_2O$) and hydromagnesite ($4MgCO_3{\cdot}Mg(OH)_2{\cdot}4H_2O$) [7]. The formation of HMCs facilitates the strength development of RMC by reducing the porosity and forming continuous network [8,9]. Therefore, RMC is a promising alternative cementitious material, potentially benefiting from lower CO_2 emissions.

Due to the importance of carbonation for RMC-based concrete, extensive research has been conducted to understand its carbonation mechanism under diverse curing conditions [10,11]. To enhance the mechanical properties of RMC concrete, efforts have also been made to identify the optimal curing conditions [4] and explore the efficacy of hydration and dispersion agents [12]. With the continuous development of RMC-based mixes, their use in various potential applications, such as non-structural blocks [4], strain-hardening composites [13,14], 3D printing matrixes [15] and high-temperature resistant concrete [16] was demonstrated. However, there has been limited investigation into the feasibility of using RMC-based mixes for structural applications.

In PC, the high alkalinity (a pH of approximately 13) of the pore solution facilitates the formation of a passive film on the surface of steel reinforcement, ensuring its long-term durability [17]. However, the passivation of the steel reinforcement is constrained in RMC-based mixes due to the relatively low pH (ranging from 9.9 to 10.5) within the matrix, resulting in a significant concern regarding its long-term performance [18]. Evidently, the corrosion of steel reinforcement in RMC-bases mixes has been observed previously [18].

To facilitate the passivation of the steel reinforcement, our previous work introduced a modest quantity of PC, enhancing the alkalinity

* Corresponding author.
E-mail address: cise.unluer@manchester.ac.uk (C. Unluer).

https://doi.org/10.1016/j.cemconcomp.2024.105668
Received 29 January 2024; Received in revised form 3 July 2024; Accepted 13 July 2024
Available online 14 July 2024

within the matrix [19]. The study revealed that by blending just 2 % of PC, the steel reinforcement could be effectively passivated, exhibiting comparable charge transfer resistance of the passive film formed in a pure PC matrix [19]. However, the strength development of RMC-based mixes is highly dependent on the formation of HMCs through carbonation [8,9], during which hydroxides are consumed, resulting in a drop of pH value within the system [20]. Consequently, the steel reinforcement is under risk for corrosion due to the low alkalinity environment after carbonation [21]. Enhancing physical properties through carbonation, while ensuring corrosion is prevented is crucial for the future structural applications of RMC-based mixes. This necessitates the detailed planning of the infrastructure needed for introducing high concentrations of CO_2 into the prepared formulations to facilitate their complete carbonation.

The carbonation of RMC-based mixes was reported to form a compact layer of carbonates, which inhibited the further diffusion of CO_2, thereby protecting the underlying matrix [22,23]. Under such circumstances, the steel reinforcement could remain a passivated state owing to the constrained extent of carbonation in the vicinity of the steel reinforcement. Nevertheless, RMC-based mixtures, varying in their proportions of PC, are likely to exhibit differing levels of porosity and alkalinity. This inherent variability within RMC-based mixes necessitates a cautious approach when attempting to extrapolate the corrosion resistance of the embedded steel reinforcement. Therefore, to facilitate the structural application of RMC-based mixes, the long-term durability of steel reinforcement under carbonation curing should be investigated.

In line with this need, the present work aims to investigate the corrosion resistance of steel reinforcement in RMC-based mixes with different proportions of PC (2 %, 20 %, and 100 % of binder component) under carbonation curing conditions. The durability of steel reinforcement embedded in mixes, where RMC was replaced by 2 %, 20 % and 100 % PC by mass were investigated. Electrochemical measurements were performed to monitor the passivation/corrosion of the steel reinforcement. The properties of the passive film were analysed by an equivalent element circuit. Given the strong interrelationship between the carbonation of cement paste and its microstructural characteristics, pore size distributions were assessed through Mercury Intrusion Porosimetry (MIP) testing. The OH^- content of the pastes at various depths was measured using pH meters. Microscale measurements, including X-ray Diffraction (XRD), Scanning Electron Microscopy (SEM) and Raman spectroscopy, were carried out to evaluate the carbonation products, microstructures of the carbonated pastes, and carbonation depth, respectively. Overall, comparison of the electrochemical behaviour, microstructural characteristics, and carbonation products of the prepared mixes led to the determination of the optimal Mg-based mix enabling the corrosion resistance of steel reinforcement. The outcome of this work can offer valuable insights in optimizing the designs of RMC-based mixes for structural applications.

2. Materials and methodology

2.1. Materials

RMC and PC used in the present study were sourced from Lingshou Minerals Processing Plant and Lafarge Cement Pte. Ltd., respectively. Both materials had relatively high purity and consistent quality. The chemical composition of RMC and PC is provided in Table 1, whereas the mix compositions can be found in Table 2. Three different binder compositions were prepared, with proportions of PC at 2 %, 20 %, and 100 %, designated as M98, M80, and M0, respectively. These proportions were determined based on our preliminary tests regarding the passivation behaviour of the steel reinforcement [19]. M0 was used as a control group to evaluate the relative performance of the other mixes under carbonation curing conditions (i.e. the observed passivity in M0 might not reflect its performance under typical field conditions).

Table 1
Chemical composition of RMC and PC.

Chemical composition (weight (%))	MgO	CaO	SiO_2	Al_2O_3	Fe_2O_3	Others
RMC	94.4	1.6	2.8	0.5	0.5	0.2
PC	3.3	62.2	24.3	4.6	4.0	1.6

Table 2
Mix compositions of M98, M80 and M0 mixes.

Mix	Binder composition		Water to binder (w/b) ratio
	RMC (%)	PC (%)	
M98	98	2	0.5
M80	80	20	
M0	0	100	

2.2. Experimental programme and sample preparation

Fig. 1 (a) depicts the assembled sample prior to carbonation. Initially, a steel reinforcement sample, with a chemical composition (wt. %) of 99.1 % Fe, 0.17 % C, 0.46 % Mn, 0.26 % Si and minor impurities, was cut from a bar with a diameter of 8 mm and a length of 10 mm. The sample was then sealed with epoxy, leaving only one side exposed to the cement with an area of ~50 mm^2, as illustrated in Fig. 1 (a). The exposed surface was polished with sandpaper up to 3000-grit and subsequently cleaned with acetone. Notably, a copper wire was connected to the sample for electrochemical measurements. The assembled samples were then embedded in the paste cast as 50 mm cubes (Fig. 1 (a)). All sides of the cube-shaped paste were sealed with wax, leaving one side unsealed to allow for the penetration of CO_2. The distances between the exposed surface of the steel sample and the unsealed side of the cube paste were fixed at 10 mm and 25 mm, forming two distinct groups, namely Group 1 (10-M0, 10-M80, 10-M98) and Group 2 (25-M0, 25-M80, 25-M98). These two sets of samples were placed in ambient conditions (28 ± 2 °C, 80 ± 5 % RH and ambient CO_2) for one day until the samples could be demoulded from the moulds. They were placed in a carbonation chamber with controlled conditions (28 ± 2 °C, 80 ± 5 % relative humidity (RH), and 20 % CO_2) for curing. During this curing process, various characterization measurements were conducted to evaluate the properties of both pastes and steel reinforcements.

2.3. Electrochemical measurements

The electrochemical measurements were conducted using a potentiostat manufactured from Princeton Applied Research (USA). A three-electrode system was employed, as depicted in Fig. 1 (b), with the steel sample serving as the working electrode, a platinum counter electrode, and a saturated calomel reference electrode. A water-saturated sponge was placed on the contact surface of the paste to facilitate the connection of the reference and counter electrodes to the working electrode. Open circuit potential (OCP) and Electrochemical impedance spectra (EIS) allow for the monitoring of passivation and corrosion processes over time. OCP was recorded every 5 s for 5 min at 0d, 1 d, 7 d, 14 d and 28 d. EIS was obtained at 7 d and 28 d, with a frequency range of 100 kHz to 0.01 Hz and an AC signal with an amplitude of 10 mV.

2.4. Pore size distribution of the paste

Mercury intrusion porosimetry (MIP) was employed to investigate the internal pore structure of the M98, M80 and M0 pastes prior to carbonation. The mercury intrusion porosimeter was manufactured from Autopore IV9510, Micromeritics, America. The samples were prepared by crushing the pastes into small particles, each with dimensions below 2 mm × 4 mm × 10 mm. The samples were then washed

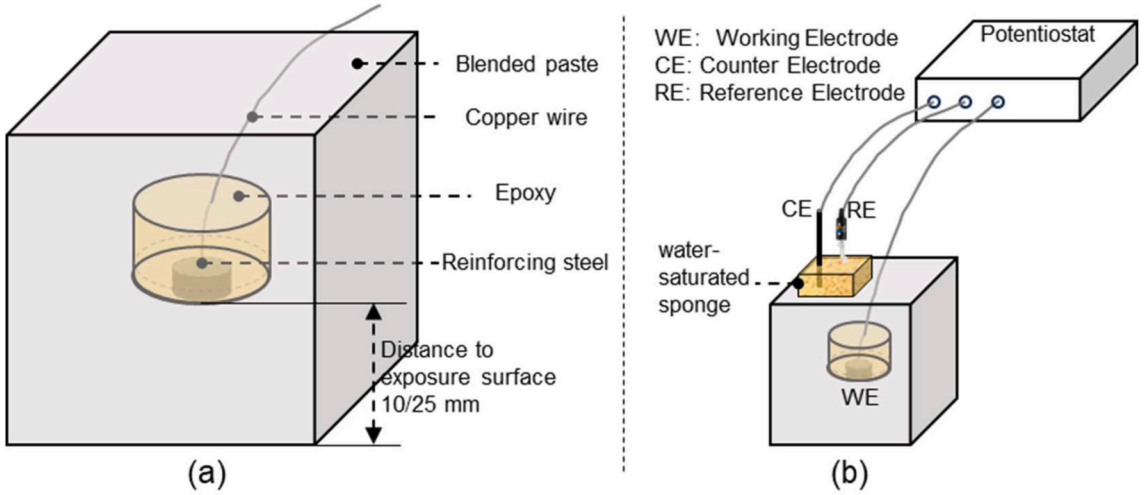

Fig. 1. Schematic diagram, demonstrating: (a) sample assembly and (b) three-electrode setup for electrochemical measurements.

by ethanol and dried in an oven at 40 °C for 48 h. Subsequently, they were sealed in preparation for the MIP test.

2.5. Chemical composition of carbonated samples

A Bruker D8 Advance instrument was employed to acquire the XRD patterns of the carbonated pastes at various depths and to characterise the chemical changes occurring in the carbonated pastes. Each XRD pattern was obtained using Cu-K_α radiation (40 kV, 40 mA) at a scanning rate of 0.04° 2θ/step, covering a range from 5° to 45° 2θ. The samples were prepared by cutting the cube paste layer-by-layer from the surface that was exposed to CO_2, targeting four specific depth intervals: 0–5 mm, 5–10 mm, 10–15 mm and 15–20 mm. Each layer was subsequently crushed into fine powders with particle sizes less than 75 μm.

2.6. Morphologies of the carbonated phases

The morphologies of the carbonated phases were characterized using a Zeiss Evo 50 microscope. The samples from different depths were initially vacuum-dried for 24 h at 40 °C and were then mounted onto the sample stage using double-sided adhesive carbon tape. The images were obtained under vacuum conditions.

2.7. Raman spectroscopy

A Renishaw inVia Raman spectrometer, equipped with a 738 nm laser, was employed to assess the carbonation depth of the pastes after carbonation, providing spatially resolved information on the distribution of carbonation products. The laser was focused via a Newport M-5X microscope objective lens with a numerical aperture (N.A.) of 0.10, resulting in a spot size of ~4 μm in diameter. Raman mapping was employed to capture the distribution of the carbonation products. Each spectrum acquired in this study was recorded with an exposure time of 10 s and two accumulations. The Raman mapping was conducted along the cross-section of the sample, with seven points sampled at intervals of 100 μm over a length of 600 μm, starting from the surface and extending to a depth of up to 11 mm.

3. Results

3.1. Electrochemical results

The open circuit potential (OCP) serves as an indicator of the passivation or corrosion status of steel reinforcement, representing the equilibrium potential between the steel reinforcement and the reference electrode [24]. Fig. 2 presents the OCP results for the steel reinforcement embedded at a depth of 10 mm. With the time of carbonation, the OCP values for 10-M0 and 10-M80 increased from ~-300 mV to ~ -150 mV at 7 d, maintaining this value consistently until 28 d. This observed behaviour aligns with the expected characteristics of the typical passivation process associated with steel reinforcement [19,25]. Alternatively, the OCP value for 10-M98 initially exhibited a substantial increase, indicating an initial passivation process [19]. However, a notable shift occurred at 7d, indicating the corrosion of the steel reinforcement embedded in 10-M98 mix [25–27]. The OCP values of the steel reinforcement embedded at a depth of 25 mm are shown in Fig. 3. The results indicate that the steel reinforcements in 25-M0 and 25-M80 underwent a passivation process, evidenced by the gradual increase in OCP values. Conversely, the steel reinforcement in 25-M98 displayed distinct behaviour, characterized by an initial increase in OCP values (rising above −100 mV) until 14 d, followed by a dramatic decline (falling below −300 mV) at 28 d. These observations collectively suggest that the steel reinforcement experienced passivation up to 14 d, followed by a subsequent corrosion process at 28 d. However, several factors, including relative humidity and oxygen availability, can influence the OCP values, thereby reducing the reliability of the results. Consequently, EIS was conducted to further evaluate the electrochemical behaviour of the steel reinforcement in different mixes.

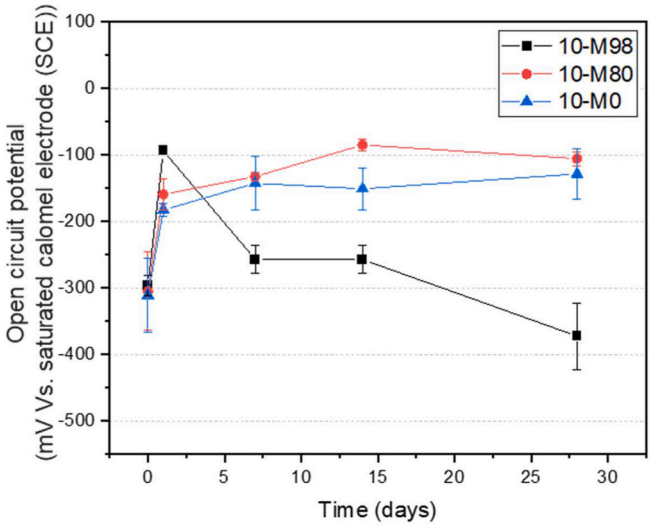

Fig. 2. OCP results of steel reinforcement at a depth of 10 mm.

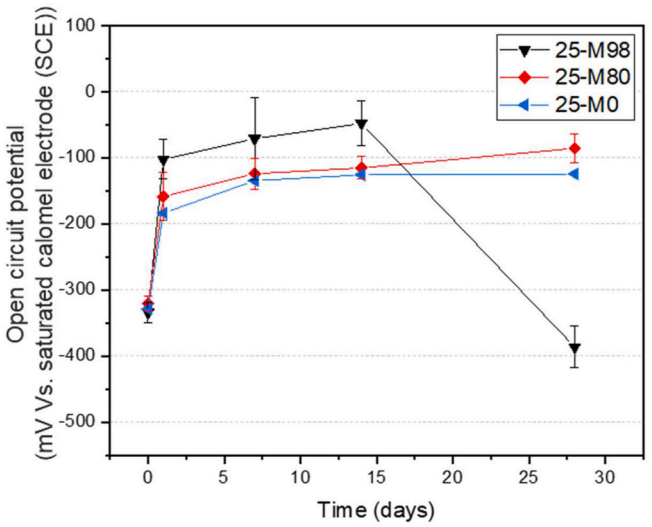

Fig. 3. OCP results of steel reinforcement at a depth of 25 mm.

The passivation or corrosion status of the steel reinforcement was further analysed by the EIS spectra as illustrated in Figs. 4 and 5. The semi-circle of the Nyquist plot represents the polarization resistance of the steel reinforcement, which could be linked to the formation of passive film/corrosion product [28]. In Fig. 4 (a), the diameter of the semi-circle of 10-M98 was the lowest at both 7 d and 28 d, with the exceedingly diminished value signifying the corrosion of the steel reinforcement. In contrast, the diameters of the semi-circles of 10-M0 and 10-M80 were increased from 7 d to 28 d, which suggests ongoing passivation processes. The observations presented in Fig. 5 (a), concerning the steel reinforcement embedded at a depth of 25 mm, generally mirrored these trends, except for 25-M98. The diameter of the semi-circle for 25-M98 at 7 days was similar to the others, but a remarkable reduction occurred at 28 days. This pattern indicates that the steel reinforcement was passivated at 7 days and subsequently underwent corrosion at 28 days, aligning with the findings observed in the OCP results. In addition to the Nyquist plots, the Bode plots are presented in Fig. 4(b–c) and 5 (b-c). The results indicated that in the high-frequency range, there was an increase in the resistance of the cement paste from 7 days to 28 days across all mixes. Furthermore, the phase angle plateaus broadened over time for the M80 and M0 mixes, suggesting the progression of passivation [29]. Furthermore, significant differences in the low-frequency range were observed, which have been reported to be influenced by the interface between the paste and the surface of the steel reinforcement [30]. To further evaluate the passivation of the steel reinforcement, an Equivalent Element Circuit (EEC) was employed in the analysis of EIS results. It should be noted that the corroded systems were not fitted due to significant resistance differences [31].

Fig. 6 presents the EEC that was employed by several researchers to fit electrochemical systems with stable passivation characteristics [19,32,33]. Furthermore, the selection of the EEC was also verified by characteristics of the Nyquist plot and the physical properties of the system. In this circuit, R_c was designated as the resistance associated with the cement paste cover, while R_f and Q_f served as the resistance and capacitance parameters of the passive film, respectively. Furthermore, R_{ct} and Q_{dl} were ascribed to the charge transfer resistance and the double layer capacitance at the steel-cement paste interface, respectively [33–35]. A constant phase element (CPE) was utilized as an alternative to the ideal capacitor [36,37]. The fitting lines were plotted in Figs. 4 and 5 and the calculated results were listed in Table 3. The value of R_c for each sample demonstrated a notable increase from 7 d to 28 d, which can be linked to the processes of hydration and carbonation within the cement paste [38,39]. Furthermore, the resistance of passive film (R_f) formed on steel reinforcement in M0 exhibited the lowest value, which is consistent with the finding in our previous work [19]. In terms of the charge transfer resistance (R_{ct}), all samples displayed comparable values, revealing a similar degree of resistance to corrosion, which should be attributed to the structure and chemical compositions of the passive film as reported in our previous work [19].

Under the conditions of accelerated carbonation, the corrosion of steel reinforcement was exclusively observed in the M98 sample, occurring at 7 d and 28 d for specimens located at depths of 10 mm and 25 mm, respectively. Alternatively, the steel reinforcement in M0 and M80 samples maintained their passivated status throughout the entire 28-day period, revealing their robust resistance to corrosion. The properties of the passive films formed on these steel reinforcements generally aligned with findings documented in our previous work [19]. Consequently, it is reasonable to suspect that the carbonation of the cement paste at the exposed surface did not significantly impact the characteristics of the passive film developed on the steel surface, particularly when the carbonation front remained at a considerable distance from the vicinity of the steel reinforcements.

3.2. *Pore distribution of pastes*

The carbonation process in cement paste is intricately linked to the microstructure of the cement paste. To investigate this relationship, pore size distributions were determined through Mercury Intrusion Porosimetry (MIP) testing, and the obtained results are presented in Fig. 7. Pores were categorized into three classes their diameters: transitional pores (ranging from 10 to 100 nm), capillary pores (encompassing diameters between 100 nm and 1.0 μm), and macropores (exceeding a diameter of 1.0 μm) [40]. Fig. 7 (a) shows the cumulative pore volume against the pore size, where M98 showed the most cumulative pore volume, revealing its maximum porosity among these three pastes. Fig. 7 (b) illustrates the log differential intrusion against the pore size, where the pore size at the major peak represented the critical pore size. The critical pore sizes of M0 and M98 were around 50 nm and 1840 nm, respectively, whereas the critical pore sizes of M80 encompassed both. The differences in the porosity should be associated with the variation in the microstructures after hydration of RMC and PC.

To gain further insights into the variations in pore structures among these pastes, the proportions of the transitional pores, capillary pores and macropores are depicted in Fig. 8. M0 exhibited the lowest macropore content and the highest proportion of transitional pores, resulting in the lowest overall porosity of 21.8 %. In contrast, M98 displayed the highest porosity of 38.0 %, with the maximum macropore content and the minimum proportion of transitional pores. It is noteworthy that all three pastes demonstrated a similar volume of capillary pores. The disparities in pore structures observed among these pastes can be attributed to the varying proportions of RMC and PC. Specifically, the hydration of RMC predominantly gives rise to macropores [41], whereas the pore structures of PC following hydration primarily consist of transitional pores [42]. Consequently, the porosity of the paste was found to increase with higher RMC content in the mixture.

3.3. *OH^- content*

Based on electrochemical results, it is evident that the onset of corrosion occurred following 7 d of carbonation. Consequently, it is imperative to gain a deeper understanding of the underlying corrosion mechanism by examining the impact of carbonation on the paste at 7 d. The OH^- contents within the paste at various depths are depicted in Fig. 9. Notably, in the cases of M0 and M80, the OH^- content within the paste exhibited substantial reductions at the 0–5 mm, which remained at a high level across subsequent depths of 5–10 mm, 10–15 mm, and 15–20 mm. This is likely attributed to the carbonation process occurring at the surface of the paste, where OH^- ions were consumed as a result of their reaction with carbonates [43]. Alternatively, the OH^- contents of

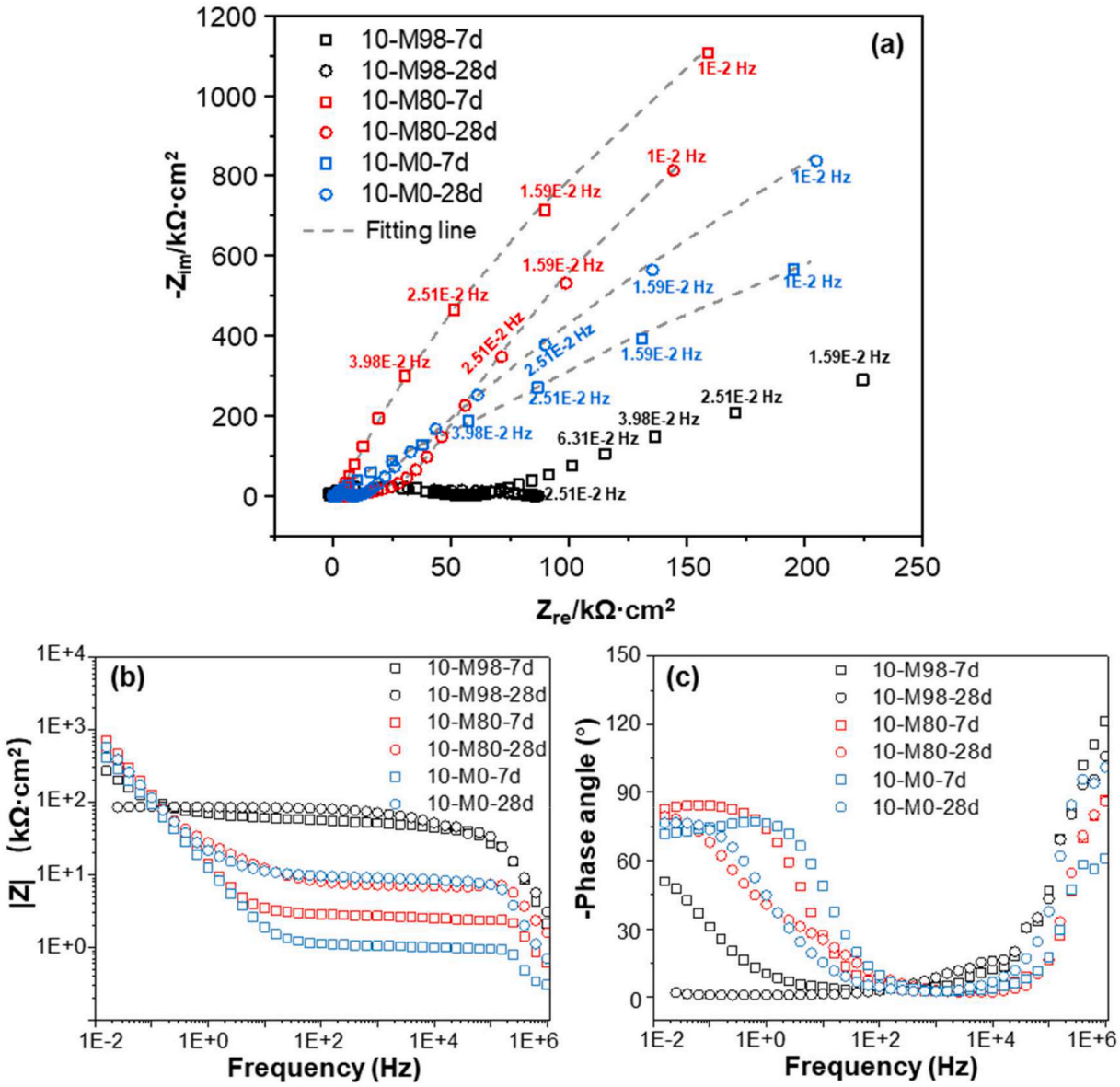

Fig. 4. EIS results of steel reinforcement at a depth of 10 mm, showing: (a) Nyquist plot along with corresponding fitting lines and (b–c) Bode plot.

paste M98 at depths of 0–5 and 5–10 displayed relatively low values, indicating a high degree of carbonation. However, at depths of 10–15 mm and 15–20 mm, the OH^- content reached similarly high levels, signifying an uncarbonated state of the paste at these deeper layers. In conclusion, under the conditions of accelerated carbonation, following 7 days, both M0 and M80 pastes underwent carbonation at depths of 0–5 mm. For M98, carbonation was observed at depths of 0–5 mm and 5–10 mm.

3.4. Chemical compositions of carbonated pastes

The chemical compositions of the paste at different depths were conducted by XRD measurements, and the results are presented in Figs. 10–12. In the case of M98, as illustrated in Fig. 10, the paste at the depths of 0–5 and 5–10 mm primarily consisted of MgO, with the most prominent peak occurring at 42.9° 2θ [44,45]. Additionally, small amounts of C_2S, C_3S, along with $Mg(OH)_2$ resulting from the hydration of MgO were detected. Furthermore, nesquehonite, hydromagnesite and calcite were identified as the principle carbonated products. At a depth of 10–15 mm, the primary compounds observed were MgO and Mg $(OH)_2$, with minor quantities of C_3S and C_2S. Notably, the peaks at 18.7° and 38.1° 2θ, indicative of $Mg(OH)_2$, were significantly reduced in the 0–10 mm depths, underscoring the depletion of $Mg(OH)_2$ due to carbonation. This observation is consistent with the substantial reduction in OH^- content noted in Fig. 9. Fig. 11 reveals the major chemical compounds in the paste M80 to be MgO, C_3S, and C_2S, along with Mg $(OH)_2$ and $Ca(OH)_2$. A comparison of the XRD patterns between 0-5 mm and 5–10 mm in the M80 paste indicates that nesquehonite and hydromagnesite were exclusively detected in the former, signifying that the carbonation front should be still within 0–5 mm depth. Additionally, a significant reduction in the intensity of the peak representing Mg $(OH)_2$/$Ca(OH)_2$ was observed at depths of 0–5 mm, attributed to the consumption of $Mg(OH)_2$/$Ca(OH)_2$ during the carbonation process. Fig. 12 provides XRD patterns for the carbonated M0 paste at depths of 0–5 mm and 5–10 mm, and they exhibit a general similarity, revealing the presence of C_3S, C_2S, Aft, and $Ca(OH)_2$. However, due to the overlapping peaks of calcite and C_3S, the exclusive presence or absence of calcite at different depths cannot be definitively ascertained based solely on the XRD results. The labelling in Fig. 12 was determined under the assumption that the carbonation front extended to a depth of 0–5 mm, in

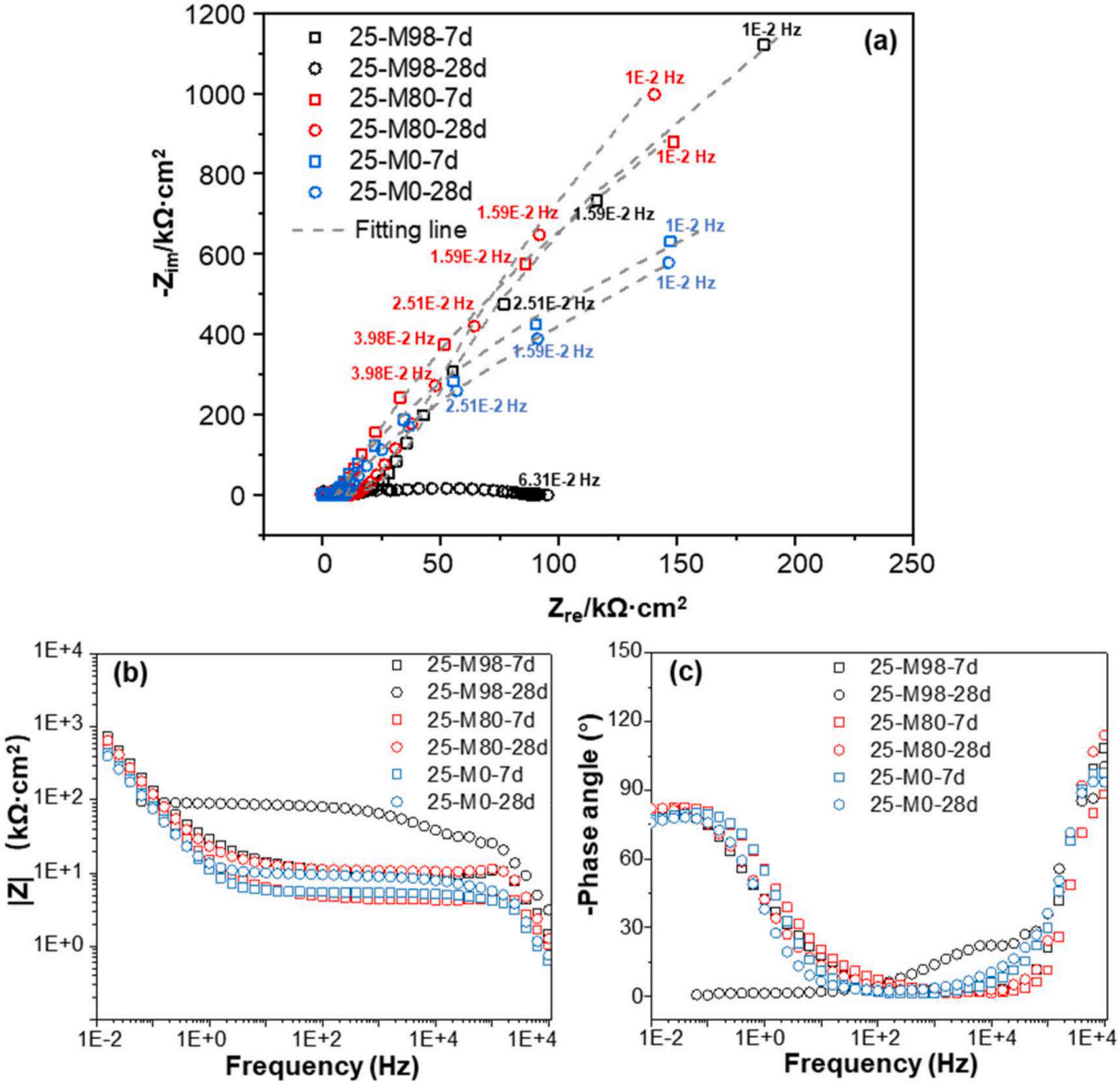

Fig. 5. EIS results of steel reinforcement at a depth of 25 mm, showing: (a) Nyquist plot along with corresponding fitting lines and (b–c) Bode plot.

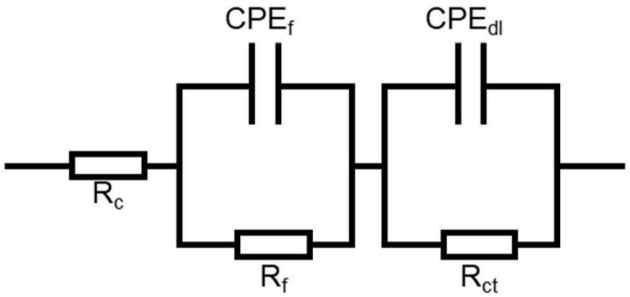

Fig. 6. Electrochemical equivalent circuit to fit EIS results.

line with the OH^- content findings presented in Fig. 9. Furthermore, Furthermore, the reduction in peak intensities at 18.0° and 26.6° 2θ clearly indicated the consumption of $Ca(OH)_2$ and C_3S, respectively. In conclusion, distinct chemical compositions were observed in different pastes, namely M0, M80, and M98, and the consumption of $Mg(OH)_2$/$Ca(OH)_2$ due to carbonation was clearly evident. However, to definitively determine the presence or absence of calcite at different depths, complementary techniques are required due to the overlapping peaks of calcite and C_3S in the XRD results.

3.5. Carbonation depth

Raman spectroscopy was employed to assess the carbonation depth of each paste at 7 days. Additionally, it also serves as a supplementary technique to discern the presence or absence of calcite at different depths, addressing the limitations of XRD measurements. As depicted in Fig. 13, distinct colours correspond to the intensities of the characteristic peaks of calcite, nesquehonite, and hydromagnesite at 1084 cm^{-1} [46], 1100 cm^{-1} [47] and 1125 cm^{-1} [48], respectively. Accordingly, the intensity, represented by the colour in Fig. 13, can be associated with the quantity of carbonated products [46,49].

Generally, the carbonation depth and products exhibited notable variations among these three pastes. In the case of M0 paste, calcite was the sole carbonation product, given the absence of RMC in its composition. The carbonation degree gradually decreased with depth, as evidenced by the colour variation, and the carbonation depth was

Table 3
Fitting results showing the value of each electrical element in different situations.

	R_c (kΩ·cm^2)	Q_f; Y_0 (Ω^{-1}·s^n/cm^2)	Q_f; n	R_f (kΩ·cm^2)	Q_{dl}; Y_0 (Ω^{-1}·s^n/cm^2)	Q_{dl}; n	R_{ct} (kΩ·cm^2)
10-M0-7d	1.95	1.45E-02	0.80	4.39E+03	1.67E-02	0.88	6.11E+04
10-M0-28d	8.70	1.10E-01	0.92	6.00E+03	1.42E-02	0.89	6.44E+04
10-M80-7d	2.71	1.26E-02	0.88	5.06E+04	1.02E-01	0.96	6.13E+04
10-M80-28d	6.90	2.28E-02	1.00	5.93E+04	2.51E-02	0.76	7.19E+04
25-M0-7d	4.40	1.47E-02	0.74	4.58E+03	3.36E-02	0.99	6.20E+04
25-M0-28d	9.07	1.83E-01	0.86	6.00E+03	1.26E-02	0.91	6.50E+04
25-M80-7d	5.51	2.16E-02	0.94	5.47E+04	4.45E-02	0.80	6.28E+04
25-M80-28d	8.98	1.11E-02	0.78	6.06E+04	2.07E-02	0.90	7.34E+04
25-M98-7d	10.03	1.93E-02	0.90	6.02E+04	2.28E-01	1.00	7.62E+04

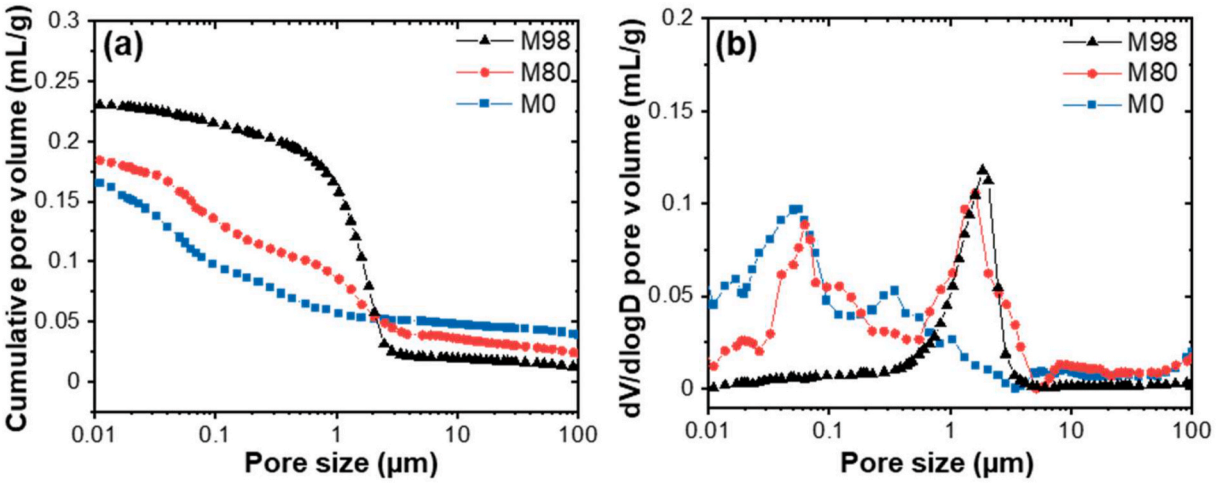

Fig. 7. MIP results, showing: (a) the cumulative pore volume against the pore size and (b) the dV/dlogD pore volume against the pore size diameter plots of different mixes.

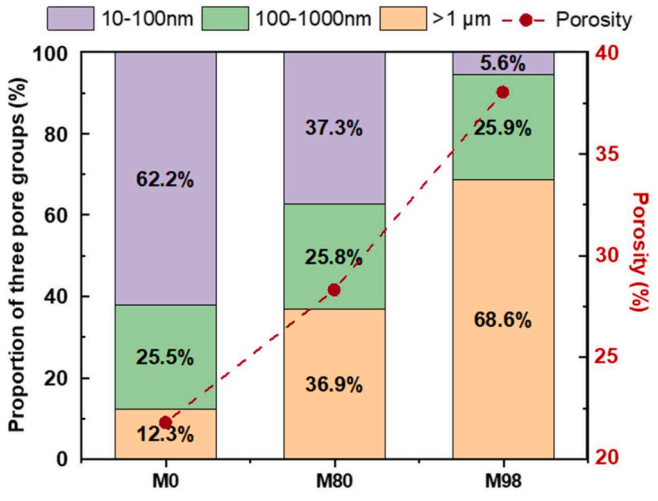

Fig. 8. Proportions of three types of pores in each mix before carbonation.

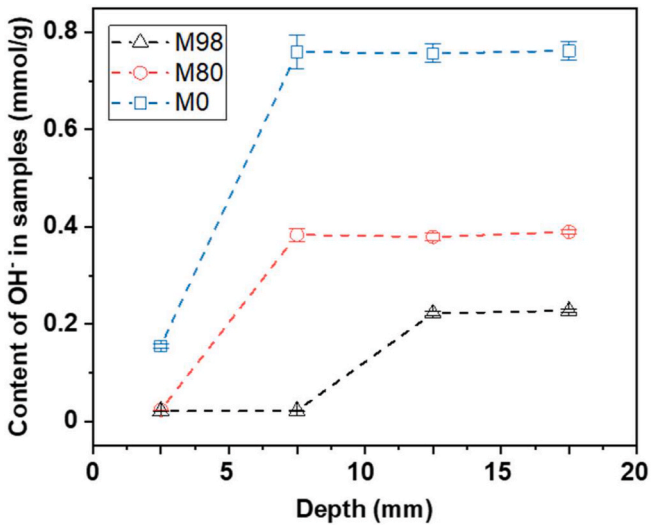

Fig. 9. OH^- content within each sample at different depths after 7 days of carbonation.

approximately 3 mm. or M80 paste, Mg-based carbonation products were also observed. Importantly, the quantity of calcite in M80 exceeded that in M0, possibly due to its higher porosity, as indicated by MIP measurements. Nonetheless, the carbonation depths of calcite, nesquehonite, and hydromagnesite in M80 were all around 3 mm, comparable to that observed in M0. This could be attributed to the formation of HMCs, which obstructed the paste's pores, hindering further CO_2 diffusion [8,50]. Alternatively, in M98 paste, the carbonation depth was significantly increased. Evidently, the depths of all three carbonation products exceeded 10 mm, with the darkest colour indicating a higher quantity than observed in both M0 and M80. This observation could be attributed to the highest porosity of M98 paste, as revealed in Fig. 7.

The carbonation depth of these three pastes can also be correlated with the electrochemical behaviour of steel reinforcement, as conducted in this study. After 7 d of carbonation, the carbonation depth in M0 and M80 did not extend beyond 10 mm. Consequently, the paste around the steel reinforcement (at a depth of 10 mm) retained a high alkalinity, maintaining the passivation status. In contrast, the carbonation depth in

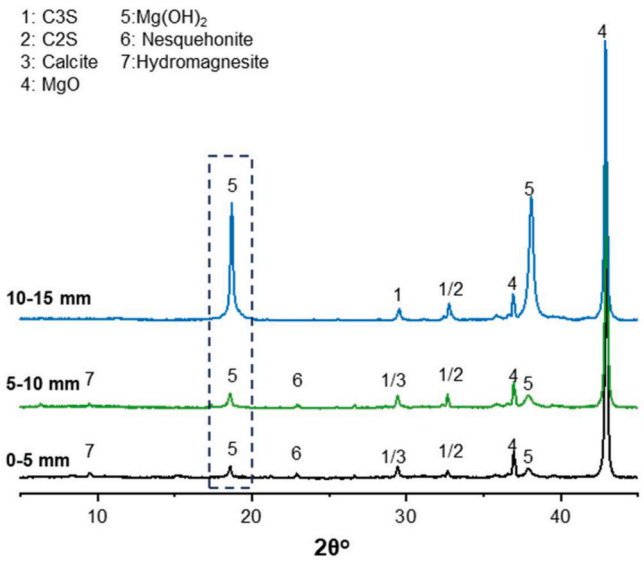

Fig. 10. XRD patterns of carbonated M98 pastes at different depths.

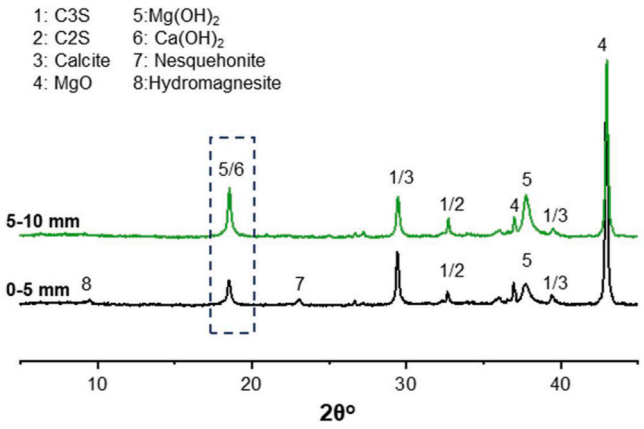

Fig. 11. XRD patterns of carbonated M80 pastes at different depths.

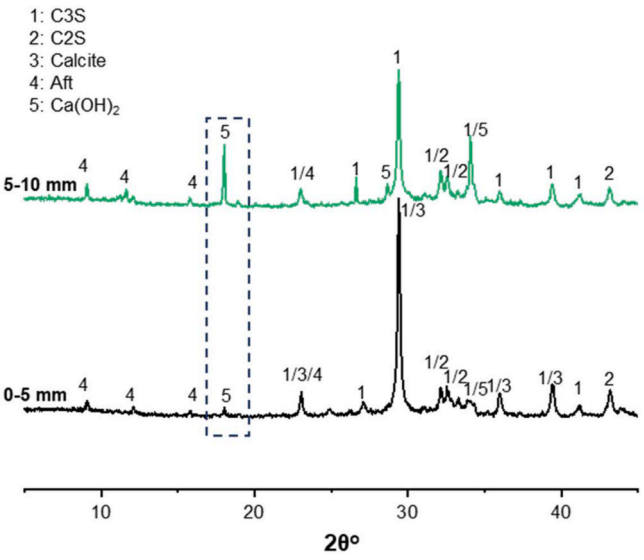

Fig. 12. XRD patterns of carbonated M0 pastes at different depths.

M98 paste reached the steel reinforcement's surface at a depth of 10 mm. The carbonation of the paste significantly reduced the alkalinity of surrounding paste [21,51], resulting in the corrosion of the steel reinforcement in M98 at 7 d. While the steel reinforcement embedded in M0 and M80 exhibited comparable corrosion resistance based on the carbonation depth, the steel reinforcement in M98 displayed limited corrosion resistance under carbonation curing. As evident in both the literature and the present study, the carbonation depth is directly linked to the condition of embedded steel reinforcement in the pastes [21].

3.6. Microstructure of carbonated pastes

To evaluate the microstructure of carbonated paste from different mixes after 7 d of carbonation, the SEM images as shown in Fig. 14 were obtained from samples at a depth of 0–5 mm. Fig. 14(a–c) illustrated the images from M0 paste. The calcite formed in carbonated paste was with relatively dense microstructures [52,53], developing on the plate-like $Ca(OH)_2$ crystals as shown in Fig. 14 (c) [54]. Apart from these two compounds, some loose particles consisting of unhydrated C_3S/C_2S and needle-like AFt [55] could be observed. The chemical compositions observed in the SEM images aligned with those found in the XRD results. Representative microstructures of carbonated M80 paste were displayed in Fig. 14(d–f). Three types of carbonation products were evident, including the polyhedron-like calcite [52], flower-like hydromagnesite [56] and needle-like nesquehonite [57,58]. Remarkably, all carbonation products were generally denser than the porous unhydrated MgO and C_3S/C_2S. In Fig. 14(g–i), the carbonated products were mainly composed of hydromagnesite and nesquehonite. Besides the carbonation products, a considerable amount of porous MgO was observed. According to the microstructures, the porosities of various carbonated pastes could be ranked as follows: M98>M80>M0, aligning with the pre-carbonation porosity ranking of these pastes.

4. Discussion

Previous literature demonstrated the stability of the passivation of steel reinforcement in all mixes (M0, M80, and M98) in the absence of carbonation [19]. However, a different scenario was observed under carbonation curing conditions, during which the corrosion resistance of the steel reinforcement embedded in RMC-based mixes exhibited significant variations, depending on the proportion of PC blended in the mixes. Present work employed a combination of XRD and Raman spectroscopy to analyse the chemical composition and carbonation depth at various intervals, providing a comprehensive understanding of the carbonation process and its effects on the paste microstructure.

Fig. 15 provides a comparative analysis of the corrosion resistance among the three investigated mixes, which could be used to support the exploration of the underlying mechanisms. To start with, the porosities of the 3 pastes significantly differed due to the varying proportions of PC blended into RMC-based mixes, which was supported by the MIP results (Section 3.2) and the findings of previous studies [8]. With an increase in PC proportion, the porosity of the pastes reduced, which was associated with the hydration of PC, resulting in a denser microstructure when compared to the hydration products of RMC [41,42]. This variance in porosity significantly influenced the diffusion of CO_2 within the pastes. Furthermore, the OH^- content within the pore solution of the pastes also played a crucial role in their carbonation resistance. Given that carbonation entailed the consumption of OH^-, a higher OH^- content offered a more robust buffering capacity against carbonation [59].

Beyond these principal factors, the initial formation of a dense layer of carbonation products could potentially improve the corrosion resistance of steel reinforcement during carbonation curing. In PC-based mixes, carbonation involves to the reaction between CO_2 and calcium-bearing components [60]. This process is initiated by the diffusion and dissolution of CO_2 into the pore solution, ultimately leading to the precipitation of calcium carbonate [61,62]. Alternatively, the

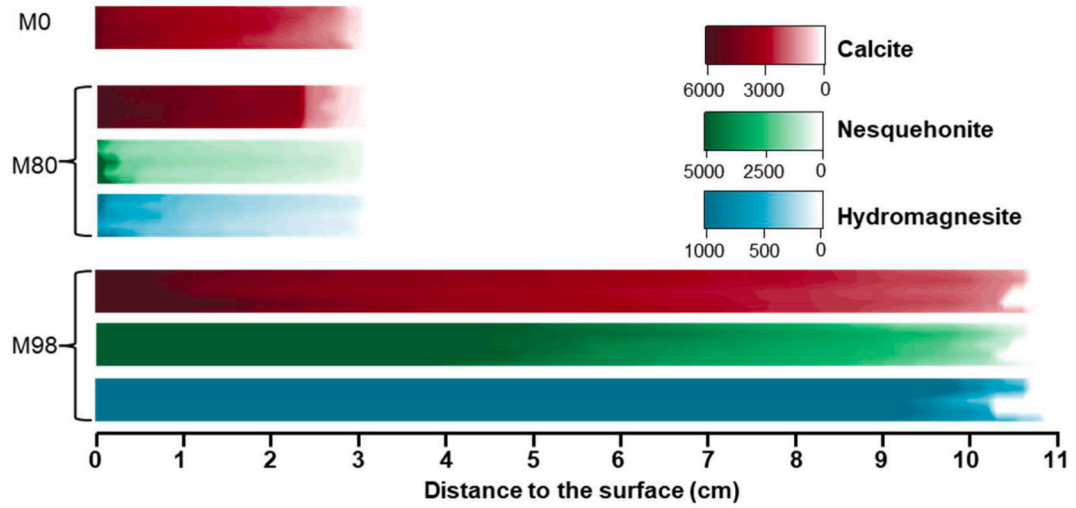

Fig. 13. Carbonation depth and carbonate phase profile of different pastes at 7 d.

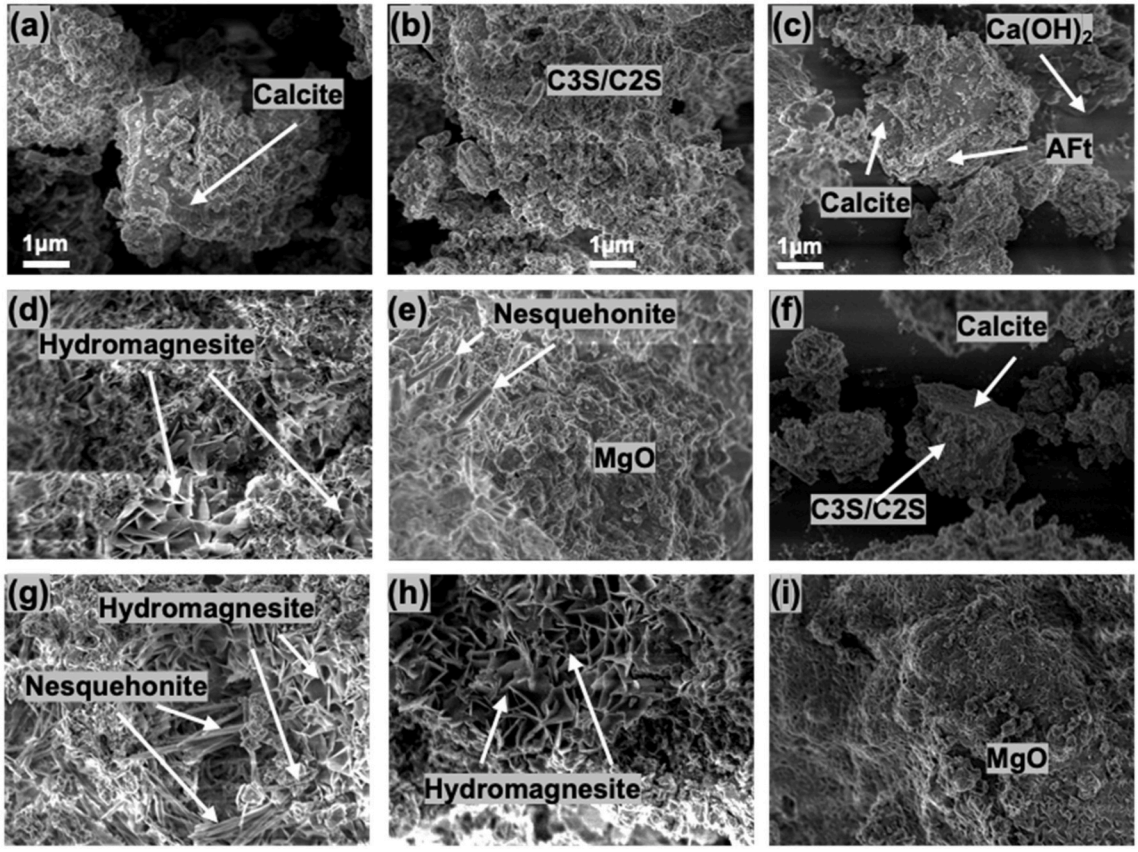

Fig. 14. SEM images obtained from carbonated pastes, showing: (a)–(c) M0, (d)–(f) M80 and (g)–(i) M98.

carbonation of RMC results in the formation of HMCs, which subsequently leads to a densified microstructure [22,23]. As a consequence, both PC and RMC carbonation yield a clogging effect on porosity, potentially forming a dense protective layer (as shown in Fig. 15) that may hinder further CO_2 diffusion and subsequent carbonation.

In light of these factors, the behaviour of steel reinforcement embedded in M0, M80, and M98 can be deduced accordingly. M98 demonstrated the lowest OH^-content, as also evidenced by its lowest pH value [19]. With the smallest OH^- content and highest porosity, the carbonation resistance of M98 was expected to be lowest, putting the embedded steel reinforcement at risk for corrosion. Evidently, this steel reinforcement in M98 experienced corrosion at depths of 10 mm and 25 mm at 7 days and 28 days, respectively. Alternatively, steel reinforcement embedded in M80 exhibited performance comparable to that in M0 (pure PC), remaining passivated under carbonation curing at both 10 mm and 25 mm. This was attributed to the clogging effect observed on the surfaces of M0 and M80 pastes due to the initial formation of carbonate phases, which established a protective layer that significantly hindered further carbonation. Alternatively, M98 failed to impede CO_2 diffusion effectively, given its relatively high porosity. Therefore, while

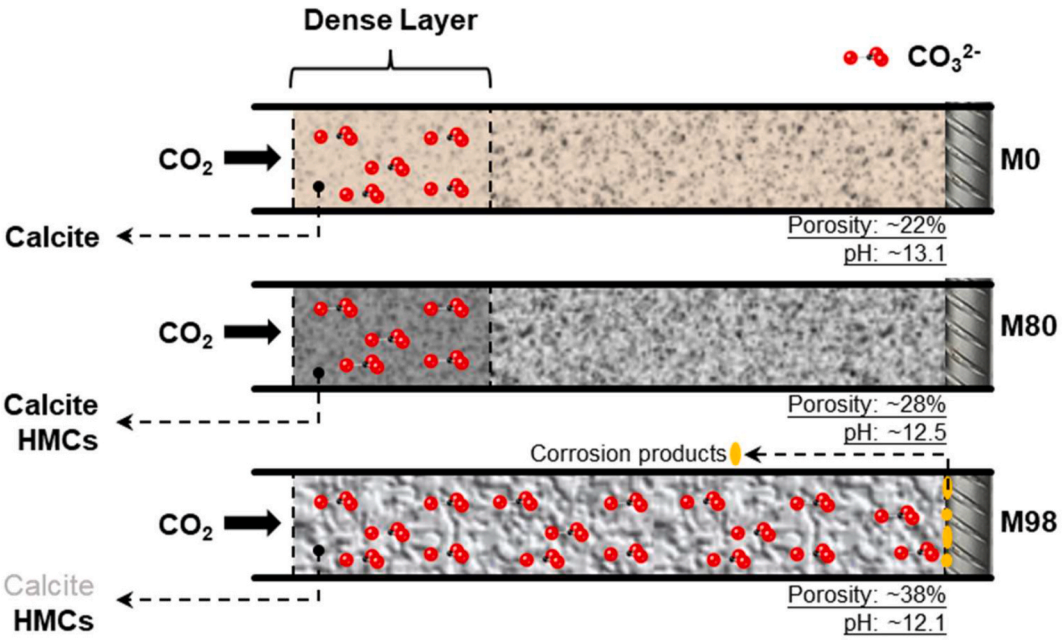

Fig. 15. Demonstration of the corrosion resistance of different samples.

steel reinforcement could be passivated in M98 without carbonation, M80 was recommended for the structural application of RMC-based mixes due to its comparable corrosion resistance to M0 under carbonation curing. It is important to note that the passivity of steel reinforcement in the M0 sample observed under carbonation conditions may not accurately reflect its performance under standard curing conditions, where the absence of accelerated carbonation could enhance its passivity.

In summary, this research underscored the viability of RMC-based mixes for structural applications. Particularly, when steel reinforcement was embedded in Mg-based mixes with 20 % PC, a relatively high corrosion resistance was demonstrated. Depending on their production conditions, the lower carbon footprint of Mg-based mixes could contribute to more sustainable construction practices, aligning with global efforts to mitigate effects of climate change. Additionally, it was shown that the formation of a compact carbonate layer could further enhance their suitability for marine applications, providing added protection in harsh environments. Apart from the practical impact of this study, the establishment of predictive models for carbonation depth and a deeper understanding of the relationship between carbonation and strength development will further enhance the practical utility of these materials, paving the way for their broader adoption in sustainable construction practices.

For future work, given the significance of accurately predicting carbonation depth in Mg-based cement paste, it is essential to conduct systematic research to establish a suitable predictive model via statistical analysis. Such a model would not only facilitate the forecasting of the service life of steel-reinforced Mg-based concrete but would also be instrumental in determining the appropriate thickness of protective cover for future structural applications. Beyond the prediction of the carbonation depth, establishing a correlation between porosity, carbonation and strength development, as well as other durability indicators such as chloride attack is also critical for the structural application of Mg-based mixes.

5. Conclusion

This study investigated the corrosion resistance of steel reinforcement in RMC-based mixes containing varying proportions of PC under carbonation curing, offering practical guidelines for enhancing the lifespan and performance of these materials in real-world applications. The feasibility of utilizing carbonated RMC-based mixes in structural applications was evaluated with respect to the changes in the corrosion mechanism in the presence of different binder compositions. The key findings of this study can be summarized as follows:

- Under carbonation curing, steel reinforcement embedded at depths of 10 mm and 25 mm in M98 was corroded at 7 d and 28 d, respectively. In contrast, steel reinforcement within M0 and M80 remained in a passivated state with comparable corrosion resistance.
- The porosities of different pastes prior to carbonation exhibited a direct correlation with the proportion of PC used in the binder component. Specifically, M98 mixture displayed the highest porosity, characterized by a majority of macropores, while M0 mixture exhibited the lowest porosity, with transitional pores as the predominant component in the microstructure.
- After 7 days of carbonation, signalling the onset of corrosion at a depth of 10 mm within M98 mixture, a decrease in the hydroxide ion (OH^-) content was observed at depths of 0–5 mm and 5–10 mm. In contrast, the reduction in OH^- content was limited to a depth of 0–5 mm in both M0 and M80 mixtures. In line with these observations, the carbonation depth in M98 mixture surpassed 10 mm, while M0 and M80 mixtures displayed carbonation depths of approximately 3 mm.
- In terms of carbonation products, M0 mixture exclusively yielded calcite; while M80 and M98 mixtures exhibited the presence of calcite, nesquehonite, and hydromagnesite. The formation of these carbonated products could explain the densification of the microstructures of these mixes.

In summary, the results of this study confirmed the feasibility to passivate steel reinforcement embedded in carbonated RMC-based mixtures in the presence of small proportions of PC. The obtained findings can provide valuable insights into the design and selection of RMC-based mixes, enhancing their suitability for various structural applications, while enabling the permanent sequestration of CO_2 in cement-based mixes via accelerated carbonation. To maximize corrosion resistance, a PC proportion of 20 % as a part of the binder component is recommended, as this concentration provides the necessary density and alkalinity for the blend to effectively resist carbonation.

CRediT authorship contribution statement

Tangwei Mi: Writing – review & editing, Writing – original draft, Validation, Methodology, Investigation, Formal analysis, Conceptualization. **En-Hua Yang:** Writing – review & editing, Writing – original draft, Supervision, Resources, Project administration, Methodology, Conceptualization. **Cise Unluer:** Writing – review & editing, Writing – original draft, Supervision, Resources, Project administration, Methodology, Conceptualization.

Declaration of competing interest

None.

Data availability

No data was used for the research described in the article.

Acknowledgements

The authors would like to acknowledge financial support from the Ministry of National Development, Singapore (CoT-V1-2020-1).

References

[1] Supriya, R. Chaudhury, U. Sharma, P.C. Thapliyal, L.P. Singh, Low-CO2 emission strategies to achieve net zero target in cement sector, J. Clean. Prod. 417 (2023) 137466.
[2] R. Zhang, A. Arrigoni, D.K. Panesar, Could reactive MgO cement be a green solution? The effect of CO2 mineralization and manufacturing route on the potential global warming impact, Cem. Concr. Compos. 124 (2021) 104263.
[3] L. Vandeperre, M. Liska, A. Al-Tabbaa, Hydration and mechanical properties of magnesia, pulverized fuel ash, and portland cement blends, J. Mater. Civ. Eng. 20 (5) (2008) 375–383.
[4] C. Unluer, A. Al-Tabbaa, Enhancing the carbonation of MgO cement porous blocks through improved curing conditions, Cement Concr. Res. 59 (2014) 55–65.
[5] F. Jin, A. Al-Tabbaa, Characterisation of different commercial reactive magnesia, Adv. Cement Res. 26 (2) (2014) 101–113.
[6] S. Ruan, E.-H. Yang, C. Unluer, Production of reactive magnesia from desalination reject brine and its use as a binder, J. CO2 Util. 44 (2021) 101383.
[7] N.T. Dung, C. Unluer, Sequestration of CO2 in reactive MgO cement-based mixes with enhanced hydration mechanisms, Construct. Build. Mater. 143 (2017) 71–82.
[8] S. Ruan, C. Unluer, Influence of mix design on the carbonation, mechanical properties and microstructure of reactive MgO cement-based concrete, Cem. Concr. Compos. 80 (2017) 104–114.
[9] N.T. Dung, C. Unluer, Development of MgO concrete with enhanced hydration and carbonation mechanisms, Cement Concr. Res. 103 (2018) 160–169.
[10] L. Mo, D.K. Panesar, Accelerated carbonation – a potential approach to sequester CO2 in cement paste containing slag and reactive MgO, Cem. Concr. Compos. 43 (2013) 69–77.
[11] E. Grünhäuser Soares, J. Castro-Gomes, Carbonation curing influencing factors of carbonated reactive magnesia cements (CRMC) – a review, J. Clean. Prod. 305 (2021) 127210.
[12] N.T. Dung, C. Unluer, Improving the performance of reactive MgO cement-based concrete mixes, Construct. Build. Mater. 126 (2016) 747–758.
[13] D. Kumar, T. Mi, E.-H. Yang, Improving the material sustainability of strain-hardening magnesium-silicate-hydrate composite by incorporating aggregates, Construct. Build. Mater. 407 (2023) 133576.
[14] H.-L. Wu, D. Zhang, B.R. Ellis, V.C. Li, Development of reactive MgO-based Engineered Cementitious Composite (ECC) through accelerated carbonation curing, Construct. Build. Mater. 191 (2018) 23–31.
[15] A. Khalil, X. Wang, K. Celik, 3D printable magnesium oxide concrete: towards sustainable modern architecture, Addit. Manuf. 33 (2020) 101145.
[16] R. Hay, N.T. Dung, A. Lesimple, C. Unluer, K. Celik, Mechanical and microstructural changes in reactive magnesium oxide cement-based concrete mixes subjected to high temperatures, Cem. Concr. Compos. 118 (2021) 103955.
[17] C.E. Locke, Corrosion of Steel in Portland Cement Concrete: Fundamental Studies, ASTM International, 1985.
[18] R. Hay, K. Celik, Hydration, carbonation, strength development and corrosion resistance of reactive MgO cement-based composites, Cement Concr. Res. 128 (2020) 105941.
[19] T. Mi, E.-H. Yang, C. Unluer, Passivation of reinforcing steel in reactive MgO cement blended with Portland cement, Cem. Concr. Compos. 143 (2023) 105269.
[20] N.T. Dung, C. Unluer, Improving the carbonation of reactive MgO cement concrete via the use of NaHCO 3 and NaCl, J. Mater. Civ. Eng. 30 (12) (2018) 04018320.
[21] A. Belda Revert, K. De Weerdt, K. Hornbostel, M.R. Geiker, Carbonation-induced corrosion: investigation of the corrosion onset, Construct. Build. Mater. 162 (2018) 847–856.
[22] N.T. Dung, A. Lesimple, R. Hay, K. Celik, C. Unluer, Formation of carbonate phases and their effect on the performance of reactive MgO cement formulations, Cement Concr. Res. 125 (2019) 105894.
[23] L. Pu, C. Unluer, Investigation of carbonation depth and its influence on the performance and microstructure of MgO cement and PC mixes, Construct. Build. Mater. 120 (2016) 349–363.
[24] A. Siddaiah, A. Kasar, R. Ramachandran, P.L. Menezes, Chapter 1 - introduction to tribocorrosion, in: A. Siddaiah, R. Ramachandran, P.L. Menezes (Eds.), Tribocorrosion, Academic Press, 2021, pp. 1–16.
[25] X.-H. Sun, X.-B. Zuo, G.-J. Yin, K. Jiang, Y.-J. Tang, Electrochemical and microscopic investigation on passive behavior of ductile iron in simulated cement-mortar pore solution, Construct. Build. Mater. 150 (Supplement C) (2017) 703–713.
[26] X. Yu, S. Al-Saadi, X.-L. Zhao, R.S. Raman, Electrochemical investigations of steels in seawater sea sand concrete environments, Materials 14 (19) (2021) 5713.
[27] B. Huet, V. L'Hostis, F. Miserque, H. Idrissi, Electrochemical behavior of mild steel in concrete: influence of pH and carbonate content of concrete pore solution, Electrochim. Acta 51 (1) (2005) 172–180.
[28] G.B. Hadjichristov, Y.G. Marinov, T.E. Vlakhov, N. Scaramuzza, Chapter Five - phospholipid Langmuir-Blodgett nano-thin monolayers: electrical response to cadmium ions and harmful volatile organic compounds, in: A. Iglič, M. Rappolt, A. J. García-Sáez (Eds.), Advances in Biomembranes and Lipid Self-Assembly, Academic Press, 2021, pp. 129–172.
[29] Y. Cai, H. Zheng, X. Hu, J. Lu, C.S. Poon, W. Li, Comparative studies on passivation and corrosion behaviors of two types of steel bars in simulated concrete pore solution, Construct. Build. Mater. 266 (2021) 120971.
[30] R. Achenbach, M. Raupach, Passivation of steel reinforcement in low carbon concrete, Buildings 14 (4) (2024) 895.
[31] G. Qiao, J. Ou, Corrosion monitoring of reinforcing steel in cement mortar by EIS and ENA, Electrochim. Acta 52 (28) (2007) 8008–8019.
[32] G. Zou, Q. Wang, G. Wang, W. Liu, S. Zhang, Z. Ai, H. Chen, H. Ma, D. Song, Revealing excellent passivation performance of a novel Cr-alloyed steel rebar in carbonized concrete environment, J. Mater. Res. Technol. 23 (2023) 1848–1861.
[33] G. Blanco, A. Bautista, H. Takenouti, EIS study of passivation of austenitic and duplex stainless steels reinforcements in simulated pore solutions, Cem. Concr. Compos. 28 (3) (2006) 212–219.
[34] F. Tang, G. Chen, R.K. Brow, Chloride-induced corrosion mechanism and rate of enamel- and epoxy-coated deformed steel bars embedded in mortar, Cement Concr. Res. 82 (2016) 58–73.
[35] W. Nguyen, J.F. Duncan, T.M. Devine, C.P. Ostertag, Electrochemical polarization and impedance of reinforced concrete and hybrid fiber-reinforced concrete under cracked matrix conditions, Electrochim. Acta 271 (2018) 319–336.
[36] M. Criado, D.M. Bastidas, S. Fajardo, A. Fernández-Jiménez, J.M. Bastidas, Corrosion behaviour of a new low-nickel stainless steel embedded in activated fly ash mortars, Cem. Concr. Compos. 33 (6) (2011) 644–652.
[37] L. Liu, S. Li, Z. Gao, H. Jia, Y. Wu, W. Hu, Effects of chloride and pH on passivation characteristics of Q235 steel in simulated concrete pore solution, Int. J. Electrochem. Sci. 17 (220648) (2022) 2.
[38] J. Zhang, F. Zheng, Z. Liu, S. Hong, B. Dong, F. Xing, Nondestructive monitoring on hydration behavior of cement pastes via the electrochemical impedance spectroscopy method, Measurement 185 (2021) 109884.
[39] L. Chi, T. Du, S. Lu, W. Li, M. Wang, Electrochemical impedance spectroscopy monitoring of hydration behaviors of cement with Na2CO3 accelerator, Construct. Build. Mater. 357 (2022) 129374.
[40] Y. Zhao, L. Peng, W. Zeng, C.s. Poon, Z. Lu, Improvement in properties of concrete with modified RCA by microbial induced carbonate precipitation, Cem. Concr. Compos. 124 (2021) 104251.
[41] H. Ma, X. Li, X. Zheng, X. Niu, Y. Fang, Effect of active MgO on the hydration kinetics characteristics and microstructures of alkali-activated fly ash-slag materials, Construct. Build. Mater. 361 (2022) 129677.
[42] C. Zhang, X. Kong, Z. Lu, D. Jansen, J. Pakusch, S. Wang, Pore structure of hardened cement paste containing colloidal polymers with varied glass transition temperature and surface charges, Cem. Concr. Compos. 95 (2019) 154–168.
[43] J. Wang, L. Xu, M. Li, H. He, Y. Wang, D. Xiang, S. Lin, Y. Zhong, H. Zhao, Effect of pre-carbonation on the properties of cement paste subjected to high temperatures, J. Build. Eng. 51 (2022) 104337.
[44] C. Pischetola, F. Hesse, J.-W.G. Bos, F. Cárdenas-Lizana, Effect of Lewis basicity on the continuous gas phase condensation of benzaldehyde with acetophenone over MgO, Appl. Catal. Gen. 623 (2021) 118277.
[45] Y.H. Taufiq-Yap, H.V. Lee, M.Z. Hussein, R. Yunus, Calcium-based mixed oxide catalysts for methanolysis of Jatropha curcas oil to biodiesel, Biomass Bioenergy 35 (2) (2011) 827–834.
[46] T. Mi, Y. Li, W. Liu, W. Li, W. Long, Z. Dong, Q. Gong, F. Xing, Y. Wang, Quantitative evaluation of cement paste carbonation using Raman spectroscopy, npj Mater. Degrad. 5 (1) (2021) 35.
[47] M.C. Hales, R.L. Frost, W.N. Martens, Thermo-Raman spectroscopy of synthetic nesquehonite—implication for the geosequestration of greenhouse gases, J. Raman Spectrosc. 39 (9) (2008) 1141–1149.
[48] R.L. Frost, Raman spectroscopic study of the magnesium carbonate mineral hydromagnesite (Mg5 [(CO3) 4 (OH) 2]· 4H2O), J. Raman Spectrosc. 42 (8) (2011) 1690–1694.
[49] P. Nie, T. Dong, S. Xiao, L. Lin, Y. He, F. Qu, Quantitative determination of thiabendazole in soil extracts by surface-enhanced Raman spectroscopy, Molecules 23 (8) (2018) 1949.
[50] N.T. Dung, C. Unluer, Performance of reactive MgO concrete under increased CO2 dissolution, Cement Concr. Res. 118 (2019) 92–101.

[51] A. Köliö, M. Honkanen, J. Lahdensivu, M. Vippola, M. Pentti, Corrosion products of carbonation induced corrosion in existing reinforced concrete facades, Cement Concr. Res. 78 (Part B) (2015) 200–207.
[52] D. Zhao, J.M. Williams, Z. Li, A.-H.A. Park, A. Radlińska, P. Hou, S. Kawashima, Hydration of cement pastes with calcium carbonate polymorphs, Cement Concr. Res. 173 (2023) 107270.
[53] I. Galan, F.P. Glasser, D. Baza, C. Andrade, Assessment of the protective effect of carbonation on portlandite crystals, Cement Concr. Res. 74 (2015) 68–77.
[54] C. Pesce, G.L. Pesce, M. Molinari, A. Richardson, Effects of organic additives on calcium hydroxide crystallisation during lime slaking, Cement Concr. Res. 139 (2021) 106254.
[55] Y. Xia, M. Liu, Y. Zhao, X. Ma, Microstructure of Portland cement blended with high dosage of sewage sludge ash activated by Na2SO4, J. Clean. Prod. 351 (2022) 131568.
[56] Y. Wang, J. Liu, T. Shi, B. Yang, C. Li, H. Xu, W. Yin, Preparation, properties and phase transition of mesoporous hydromagnesite with various morphologies from natural magnesite, Powder Technol. 364 (2020) 822–830.
[57] S. Lu, P. Yan, Y. Gao, C. Zhang, J. Lu, Insights into the structures, energies and electronic properties of nesquehonite surfaces by first-principles calculations, Adv. Powder Technol. 31 (8) (2020) 3465–3473.
[58] Q. Chen, T. Hui, H. Sun, T. Peng, W. Ding, Synthesis of magnesium carbonate hydrate from natural talc, Open Chem. 18 (1) (2020) 951–961.
[59] S. von Greve-Dierfeld, B. Lothenbach, A. Vollpracht, B. Wu, B. Huet, C. Andrade, C. Medina, C. Thiel, E. Gruyaert, H. Vanoutrive, Understanding the carbonation of concrete with supplementary cementitious materials: a critical review by RILEM TC 281-CCC, Mater. Struct. 53 (6) (2020) 136.
[60] B. Šavija, M. Luković, Carbonation of cement paste: understanding, challenges, and opportunities, Construct. Build. Mater. 117 (2016) 285–301.
[61] Q. Zhang, P. Feng, X. Shen, J. Lu, S. Ye, H. Wang, T. Ling, Q. Ran, Utilization of solid wastes to sequestrate carbon dioxide in cement-based materials and methods to improve carbonation degree: a review, J. CO2 Util. 72 (2023) 102502.
[62] C. Andrade, M.Á. Sanjuán, Carbon dioxide uptake by pure Portland and blended cement pastes, Developments in the Built Environment 8 (2021) 100063.